Supplementary information

of

Bidirectional electron donation in Cu_1−Ti pairs on TiO_x for efficient nitric oxide electroreduction

Yan Zhang[1‡], Ning Yan[2‡], Bing Zhou[1‡], Guangming Zhan[3], Jiaxian Wang[1], Long Zhao[1], Lufa Hu[1], Kaiyuan Wang[1], Junzhou Xu[1], Ke Cheng[1], Lingzhi Zhou[1], Xiang-Kui Gu[2], Yancai Yao[1]*, and Lizhi Zhang[1]

[1]School of Environmental Science and Engineering, Shanghai Jiao Tong University, Shanghai 200240, China.

[2]School of Power and Mechanical Engineering, Wuhan University, Wuhan 430072, P. R. China.

[3]Key Laboratory of Geographic Information Science of the Ministry of Education, School of Geographic Sciences, East China Normal University, Shanghai 200241, China.

[‡]Y. Z., N. Y. and B. Z. contributed equally to this work.

*Correspondence to: yyancai@sjtu.edu.cn

Supplementary Figures

Adsorption Configuration	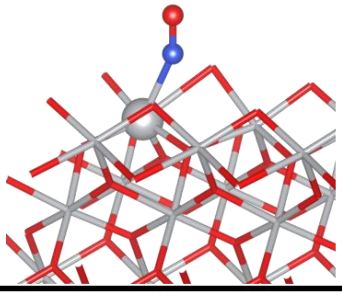
ΔE_{ads}	-1.67 eV

Supplementary Fig. 1 The adsorption structure of NO on Ti−Ti pairs. Gray, red and blue balls represent Ti, O, and N, respectively.

Adsorption Configuration	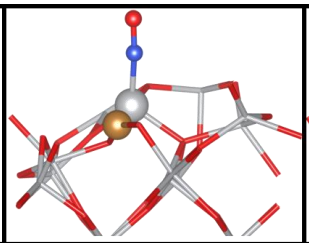	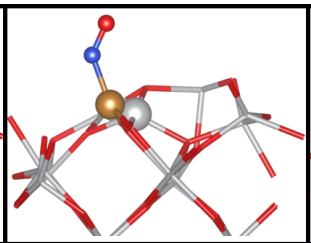	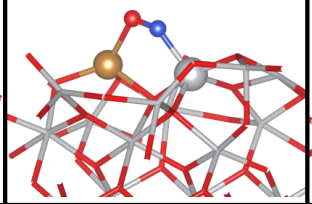	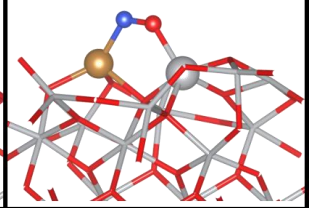
ΔE_{ads}	-1.78 eV	-1.54 eV	-1.90 eV	-1.78 eV

Supplementary Fig. 2 Adsorption configurations of NO on the surface of Cu_1−Ti pairs. Gray, red, orange and blue balls represent Ti, O, Cu and N, respectively.

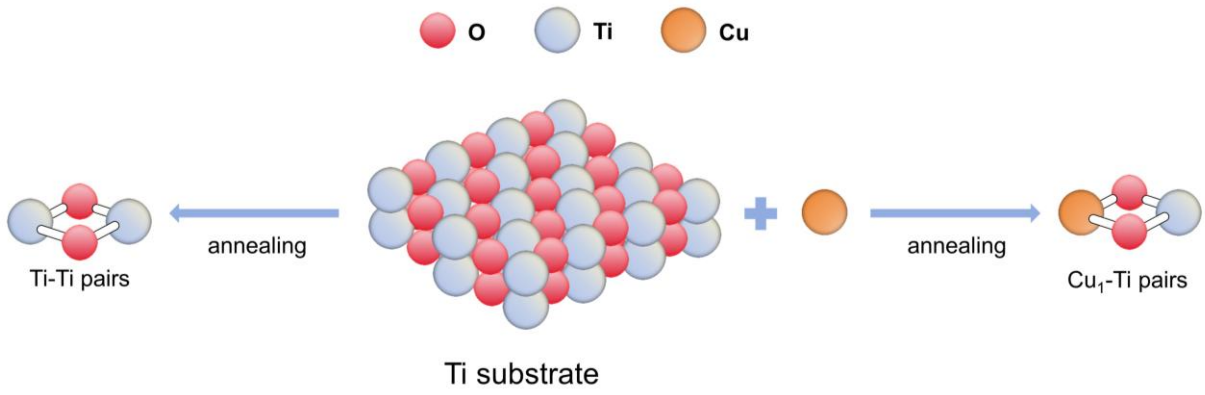

Supplementary Fig. 3 The typical synthesis route of Ti−Ti pairs and Cu_1−Ti pairs electrodes. Color code: Ti (blue), Cu (orange), and O (red).

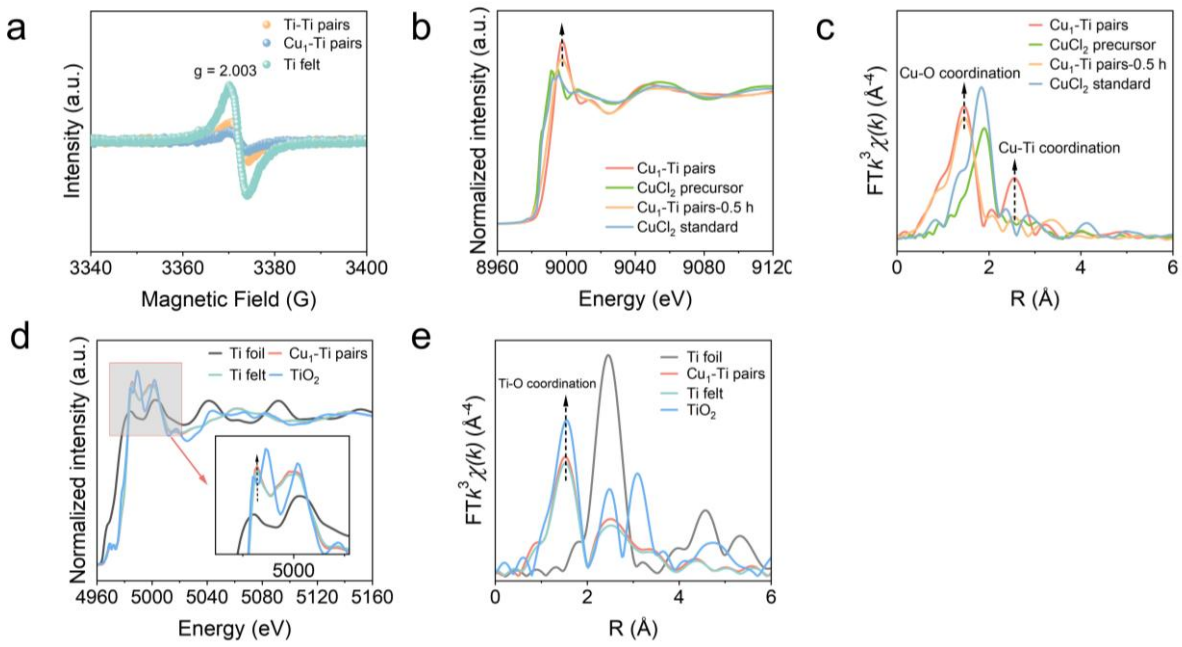

Supplementary Fig. 4 (a) EPR spectra of Ti felt, Ti−Ti pairs, and Cu_1−Ti pairs. The OVs exist on the surface of Ti felt. (b) XANES spectra and (c) FT EXAFS spectra of Cu_1−Ti pairs, $CuCl_2$ precursor, Cu_1−Ti pairs-0.5 h, and $CuCl_2$ standard sample at the Cu K-edge. (d) XANES spectra and (e) FT EXAFS spectra of Ti foil, Cu_1−Ti pairs, Ti felt, and TiO_2 at the Ti K-edge. Source data for Supplementary Fig. 4 are provided as a Source Data file.

To elucidate the formation mechanism, we performed EPR spectra, *ex situ* Ti K-edge XAFS and Cu K-edge XAFS. As shown in EPR spectra (Supplementary Fig. 4a), the surface on the pristine Ti felt was enriched with OVs. After heat treatment, the concentration of OVs on the surface of Ti–Ti pairs decreased, and further declined after the formation of Cu_1–Ti pairs, indicating that Cu atoms occupy the OVs sites.

We further performed *ex situ* Cu K-edge XAFS to trace the coordination environment evolution of Cu during the synthesis of Cu_1–Ti pairs (Supplementary Fig. 4b). The tested samples included the $CuCl_2$ precursor, the intermediate sample annealed for 0.5 h (donated as Cu_1–Ti pairs-0.5 h) and the final catalyst annealed for 3 h (Cu_1–Ti pairs). As shown in Supplementary Fig. 4c, the dominated peak for $CuCl_2$ precursor was at 1.90 Å, ascribing to the Cu–Cl coordination. In contrast, the peak for Cu_1–Ti pairs-0.5 h shifted to 1.47 Å,

corresponding to the Cu–O coordination. Combined with results of EPR and *ex situ* Cu K-edge XAFS, we believed that Cu atoms migrated into OV sites and transformed from Cu–Cl to Cu–O coordination.

With increasing annealing time from 0.5 h to 3 h under an oxygen-containing atmosphere, the Cu–O coordination was further intensified, and the Cu–Ti scattering peak in the second shell was significantly enhanced. This observation can be rationalized by the incorporation of oxygen atoms from O_2 molecules, which bridge Cu and adjacent Ti atoms at elevated temperatures, promoting the formation of stable Cu_1–Ti local structures. Meanwhile, *ex situ* Ti K-edge XAFS results (Supplementary Figs. 4d-e) further corroborated these findings. The Ti–O coordination as well as the Ti-O-Ti/Cu scattering feature in the Cu_1–Ti pairs is considerably stronger than that in the pristine Ti felt.

Combined the results from EPR and *ex situ* Ti/Cu K-edge XAFS, we could conclude that the formation mechanism that Cu^{2+} are initially trapped by OV sites, lose their Cl ligands to bond with O atoms, and then gradually interact with adjacent Ti atoms to form stable Cu_1–Ti pairs as annealing proceeds.

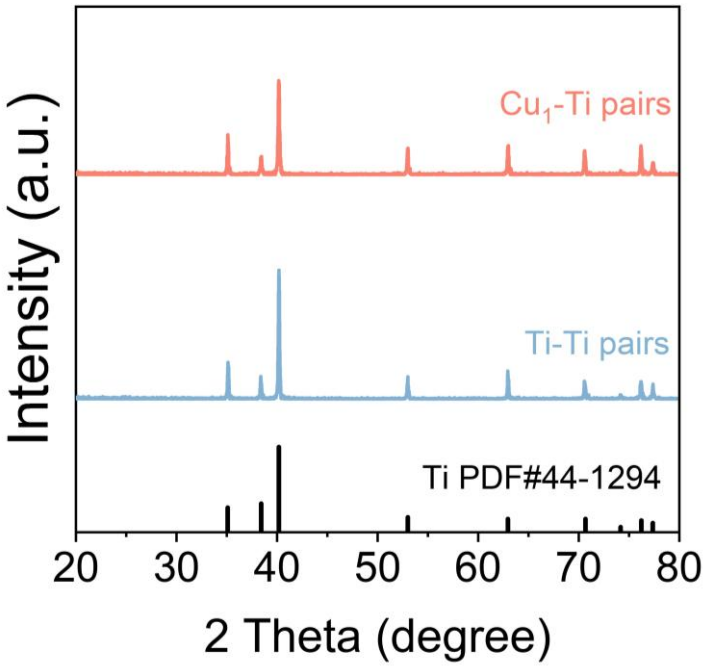

Supplementary Fig. 5 XRD patterns of Ti−Ti pairs and Cu_1−Ti pairs. Source data for Supplementary Fig. 5 are provided as a Source Data file.

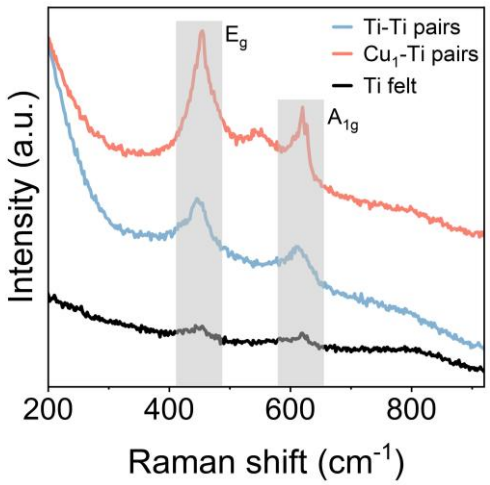

Supplementary Fig. 6 The Raman spectra of Ti felt, Ti−Ti pairs, and Cu_1−Ti pairs. The peaks at 450 and 620 cm^{-1} could be attributed to the E_g (vibrational oxygen ions in the octahedra) and A_{1g} (motion of TiO_6) vibrational modes of rutile. The enhancement of the E_g and A_{1g} modes confirmed the strengthening of the Ti−O−Ti structure induced by the reduction of OVs. Source data for Supplementary Fig. 6 are provided as a Source Data file.

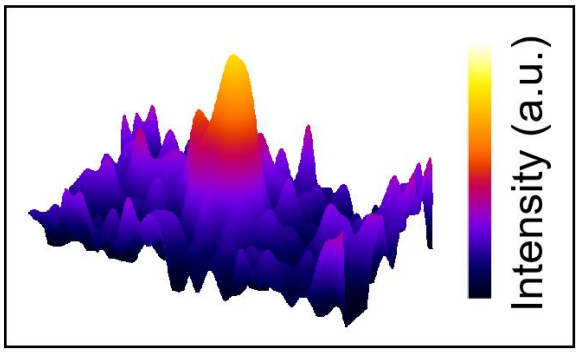

Supplementary Fig. 7 The corresponding line intensity profile of Cu_1−Ti pairs in **Fig. 1d**

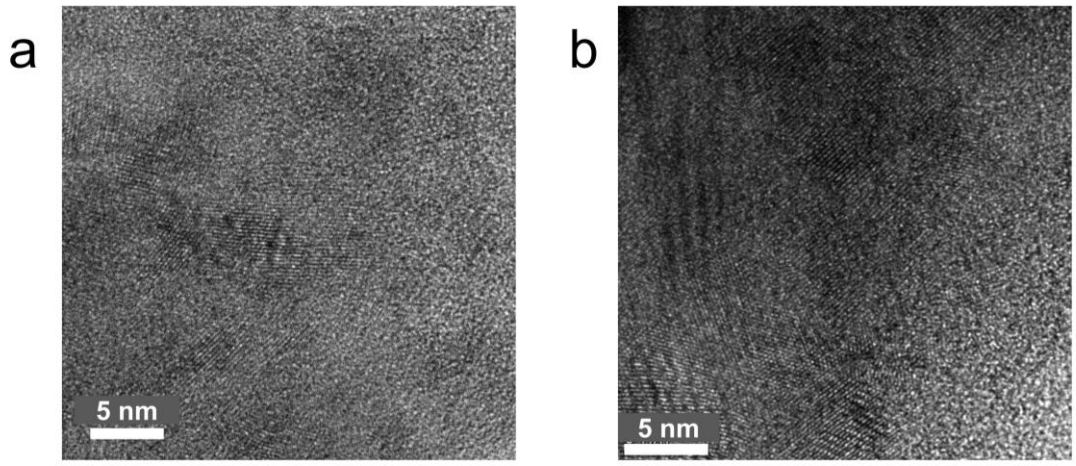

Supplementary Fig. 8 High-resolution TEM (HRTEM) images of (a) Ti−Ti pairs and (b) Cu_1−Ti pairs.

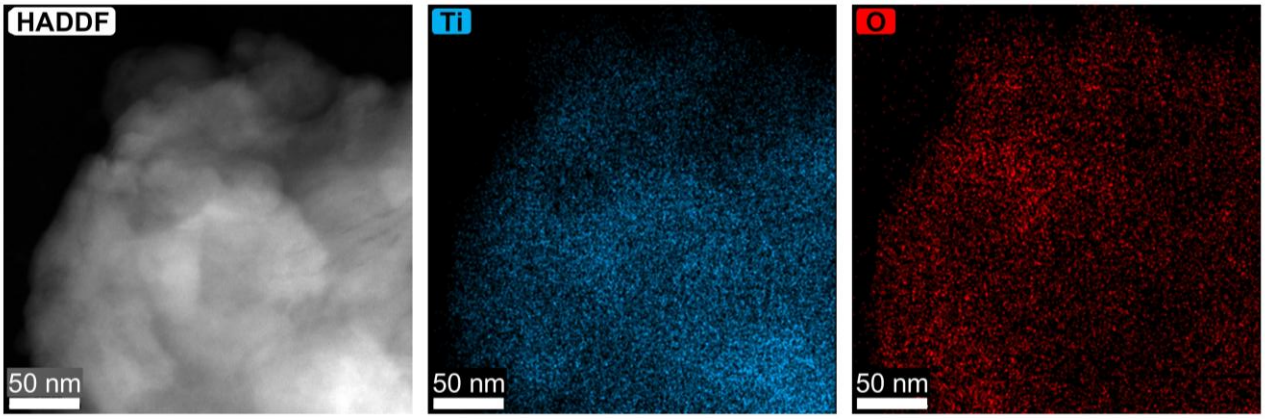

Supplementary Fig. 9 HADDF image and STEM elemental mapping of Ti−Ti pairs.

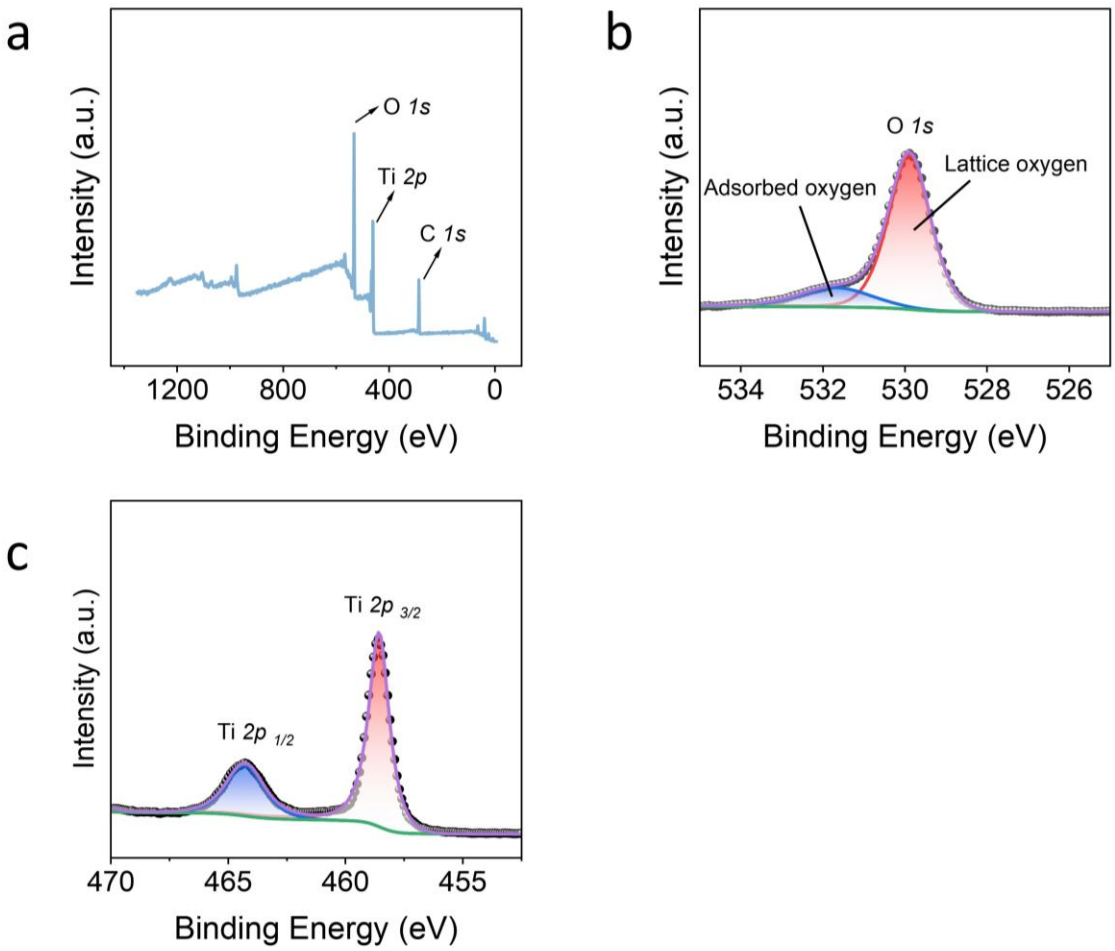

Supplementary Fig. 10 X-ray photoelectron spectroscopy (XPS) of Ti−Ti pairs. (a) Survey scan. (b) O *1s* region. (c) Ti *2p* region. Source data for Supplementary Fig. 10 are provided as a Source Data file.

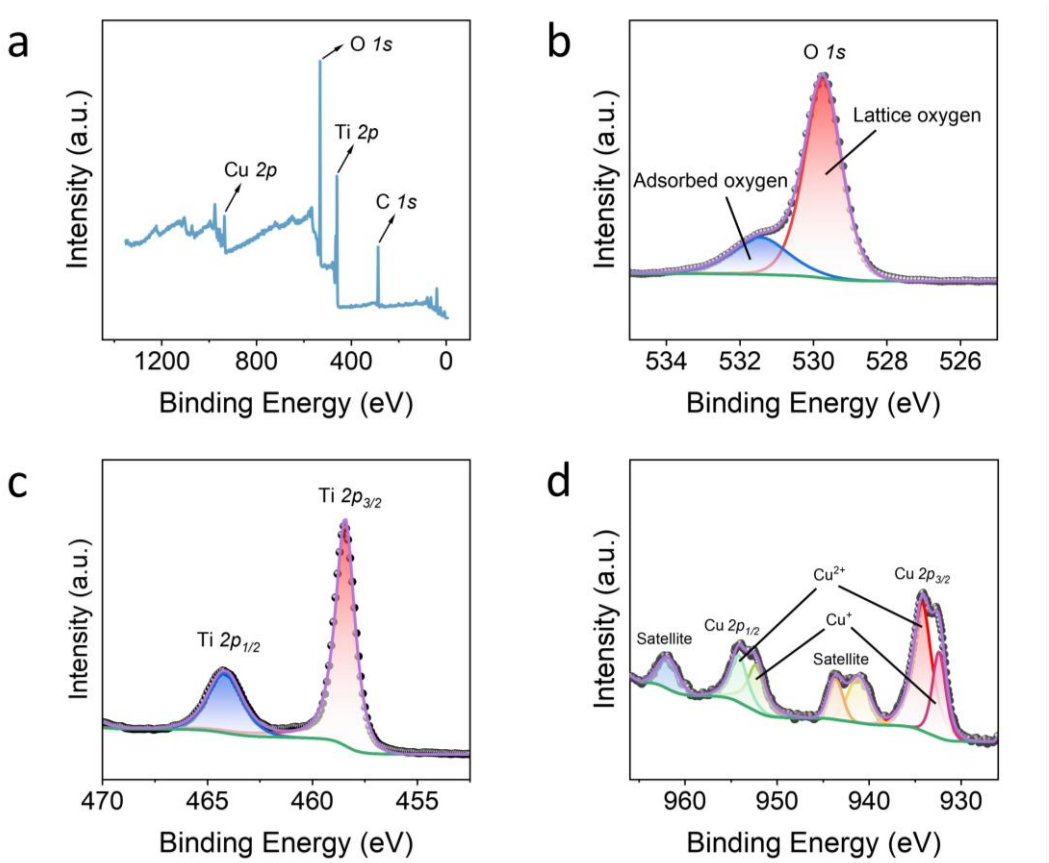

Supplementary Fig. 11 X-ray photoelectron spectroscopy (XPS) of Cu_1−Ti pairs. (a) Survey scan. (b) O *1s* region. (c) Ti *2p* region. (d) Cu *2p* region. Source data for Supplementary Fig. 11 are provided as a Source Data file.

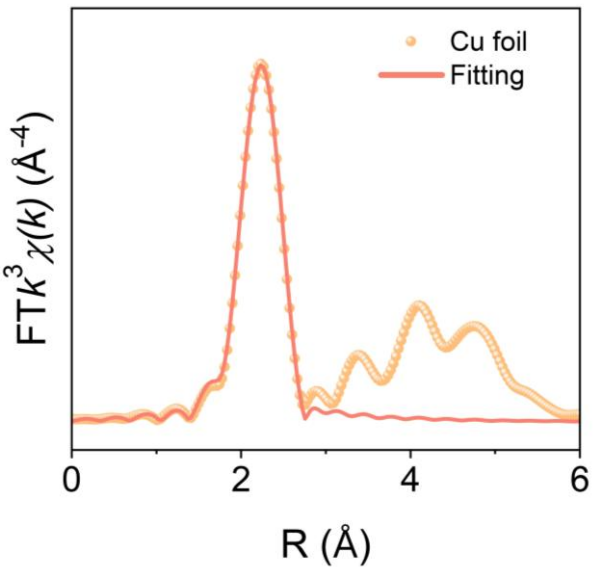

Supplementary Fig. 12 The fitting results of EXAFS. R space fitting curves at the Cu K-edge of Cu foil. It was found that the fitting curves matched quite well with the experimental spectra. Source data for Supplementary Fig. 12 are provided as a Source Data file.

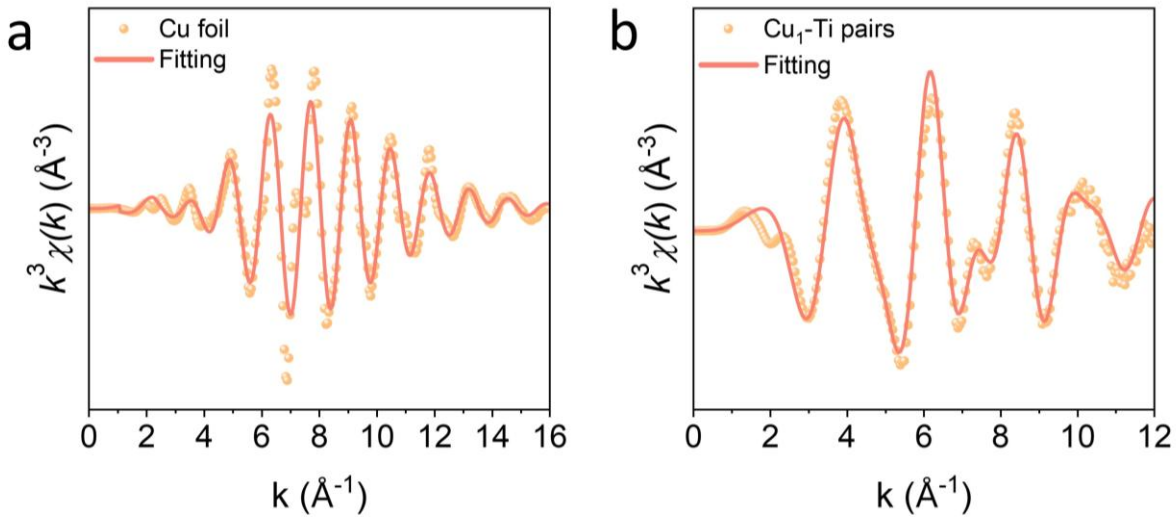

Supplementary Fig. 13 EXAFS oscillations at k^3-weighted Cu k-edge and fitted curves of (a) Cu foil and (b) Cu_1−Ti pairs. The fitting curve of k-space was in good agreement with the original data, thus confirming the accuracy of EXAFS fitting results. Source data for Supplementary Fig. 13 are provided as a Source Data file.

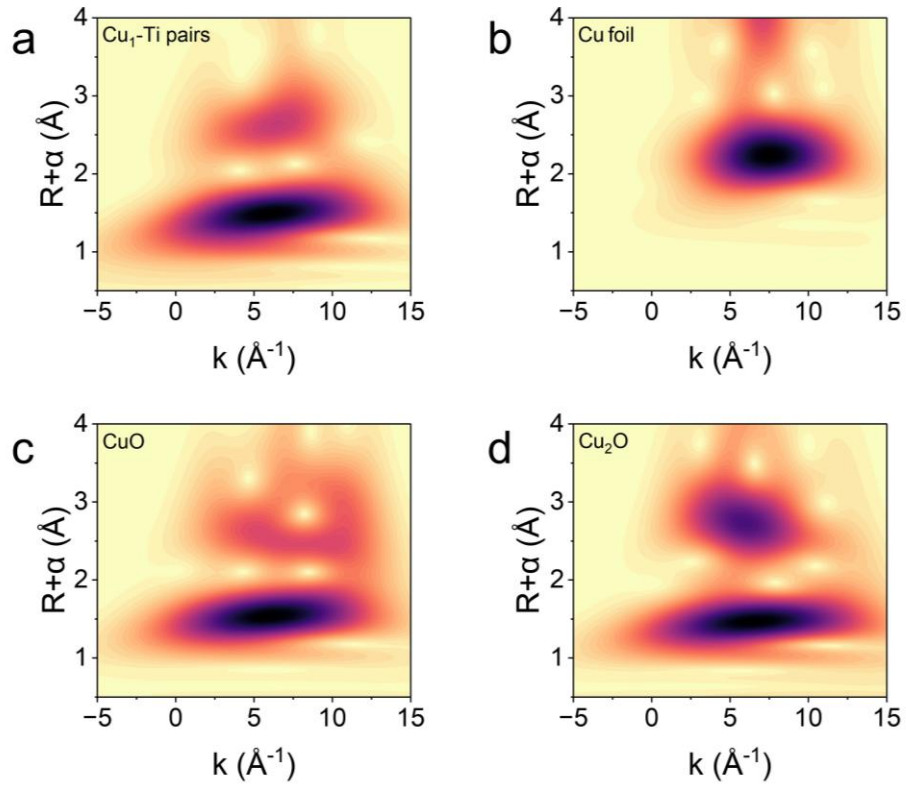

Supplementary Fig. 14 Wavelet transforms profiles of (a) Cu_1−Ti pairs and reference samples of (b) Cu foil, (c) CuO, and (d) Cu_2O. Source data for Supplementary Fig. 14 are provided as a Source Data file.

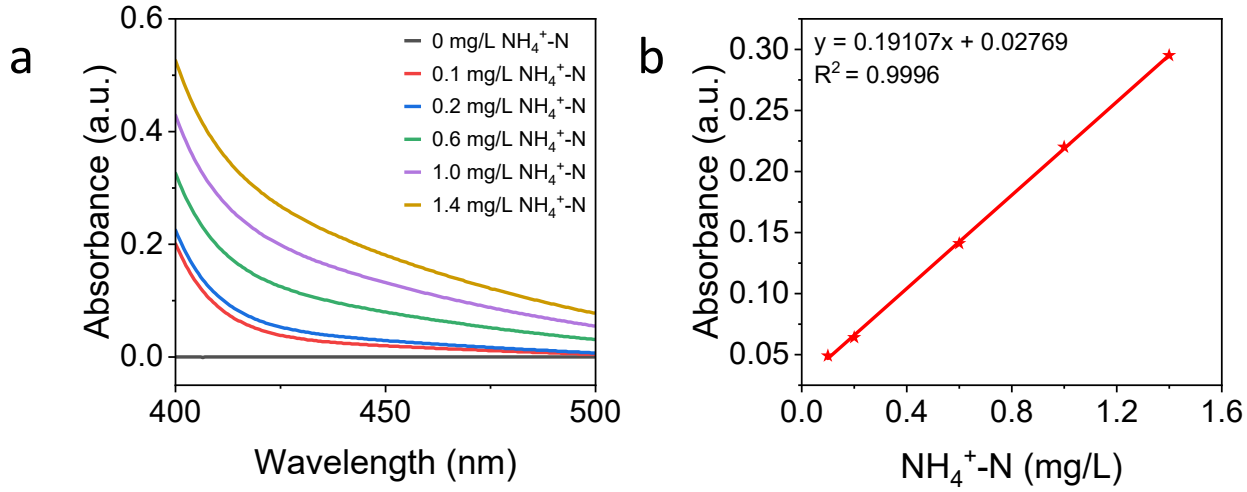

87

88 **Supplementary Fig. 15** (a) Ultraviolet-visible (UV-Vis) absorption spectra of NH_4^+ assays. (b) Calibration

89 curve used for the calculation of NH_3 concentrations. Source data for Supplementary Fig. 15 are provided as a

90 Source Data file.

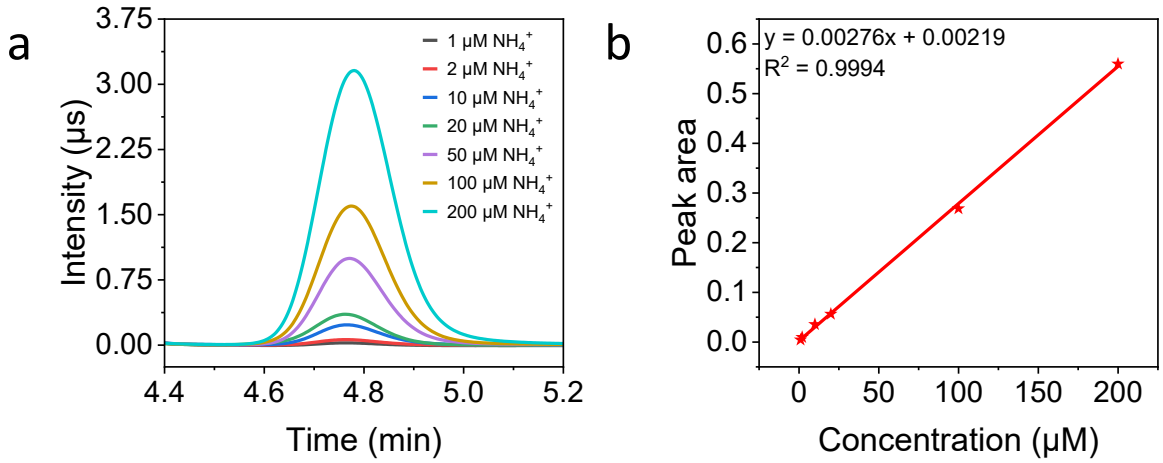

Supplementary Fig. 16 (a) Ion chromatography (IC) spectra of NH_4^+ at different concentrations. (b) The concentration-peak area standard curves of NH_3. Source data for Supplementary Fig. 16 are provided as a Source Data file.

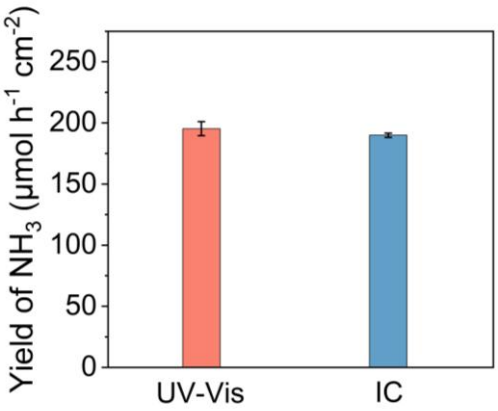

Supplementary Fig. 17 NH_3 yield obtained from UV-Vis and IC methods at −0.6 V_{RHE}. The results show that the NH_3 yield determined by IC quantitative analysis is very close to the calculated result by the colorimetric method. The error bars correspond to the standard deviation of three times of NORR measurements. Source data for Supplementary Fig. 17 are provided as a Source Data file.

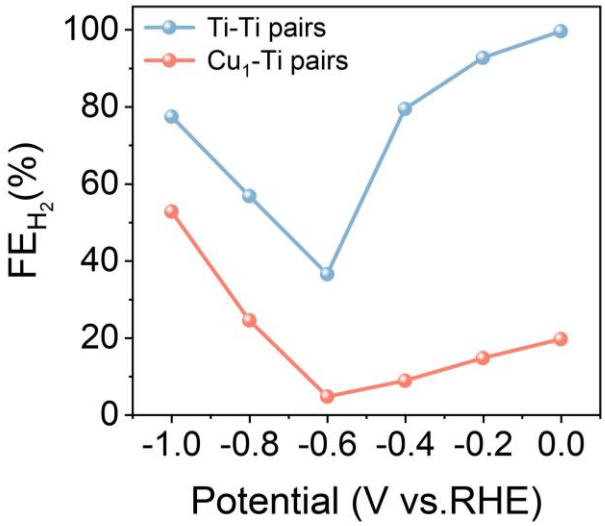

Supplementary Fig. 18 FE_{H2} of Ti−Ti pairs and Cu_1−Ti pairs within the given potential range at 25 ℃ (without iR-correction). Source data for Supplementary Fig. 18 are provided as a Source Data file.

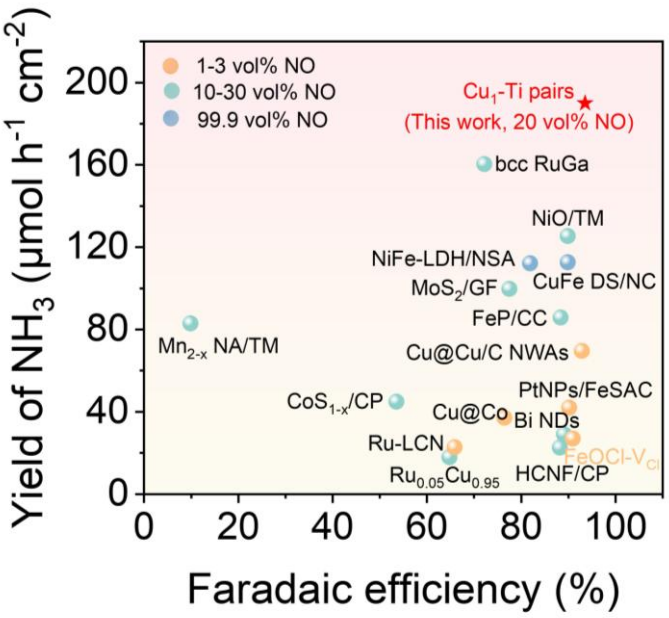

104

105 **Supplementary Fig. 19** Comparisons of the NORR performance of Cu_1−Ti pairs with other previously reported

106 electrocatalysts. Source data for Supplementary Fig. 19 are provided as a Source Data file.

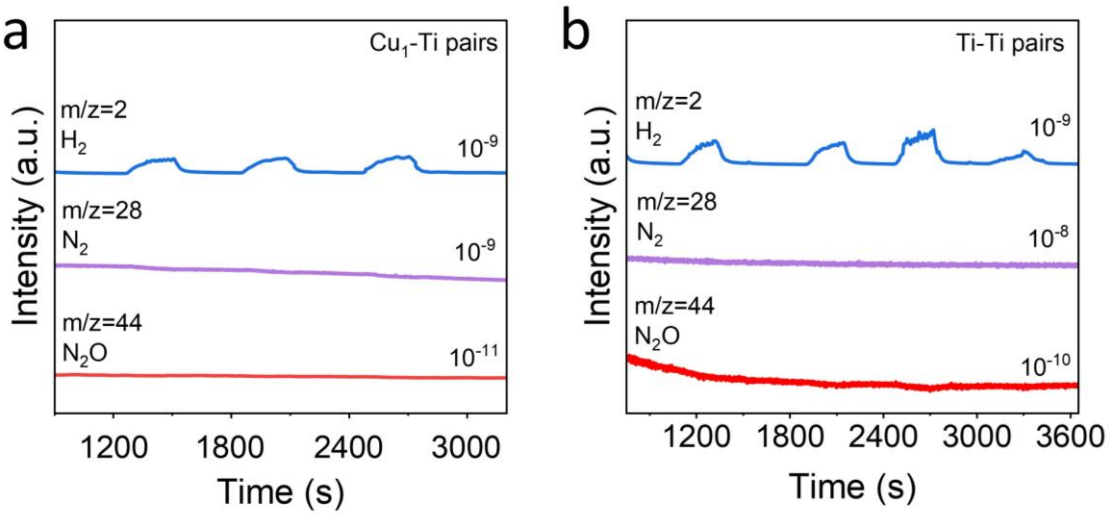

Supplementary Fig. 20 The signal spectrum of the intermediates on (a) Cu_1−Ti pairs and (b) Ti−Ti pairs monitored by DEMS during the NORR. No characteristic signals corresponding to N_2 or N_2O were detected for either the Cu_1−Ti pairs or Ti−Ti pairs, suggesting that N_2 and N_2O were not generated during the NORR. Source data for Supplementary Fig. 20 are provided as a Source Data file.

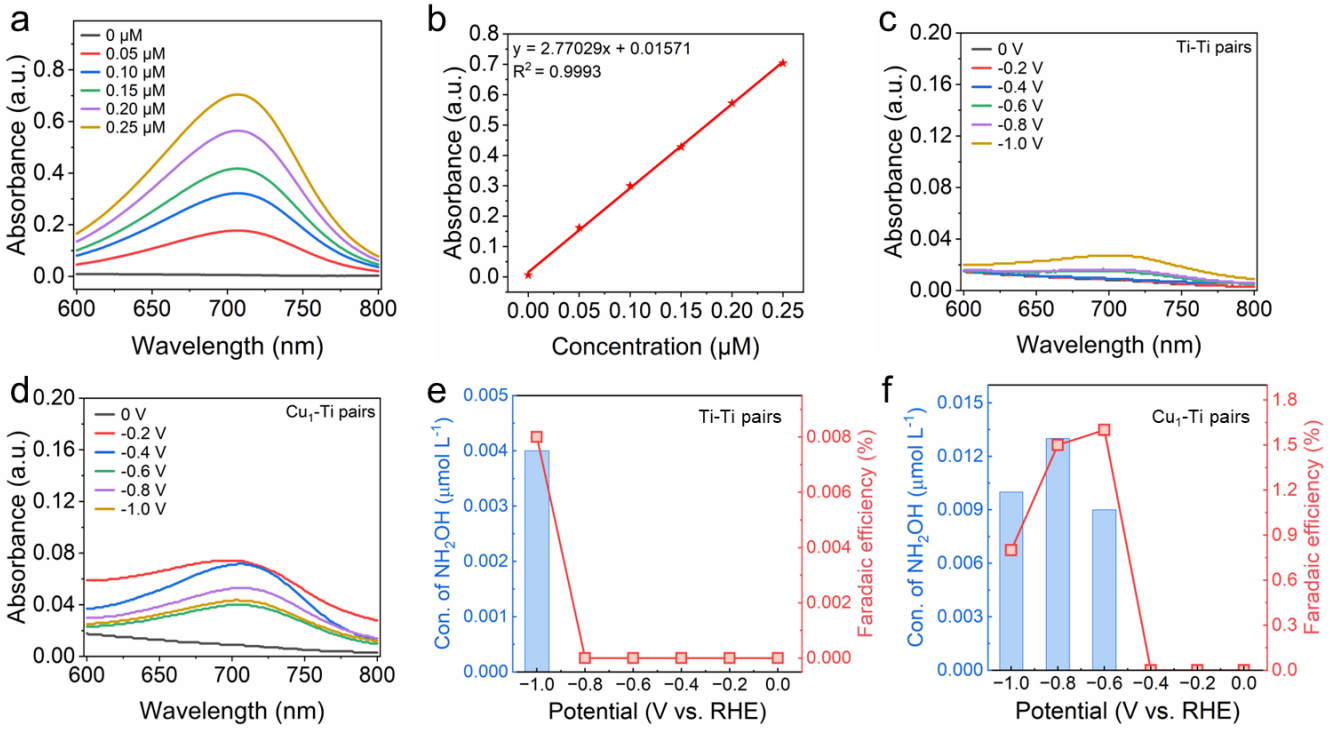

Supplementary Fig. 21 (a) UV-Vis absorption spectra of NH_2OH assays. (b) Calibration curve for quantitative calculation of NH_2OH concentrations. UV-Vis spectra for NH_2OH produced by (c) Ti−Ti pairs and (d) Cu_1−Ti. Corresponding NH_2OH concentration and Faradaic efficiency of (e) Ti−Ti and (f) Cu_1−Ti pairs. Source data for Supplementary Fig. 21 are provided as a Source Data file.

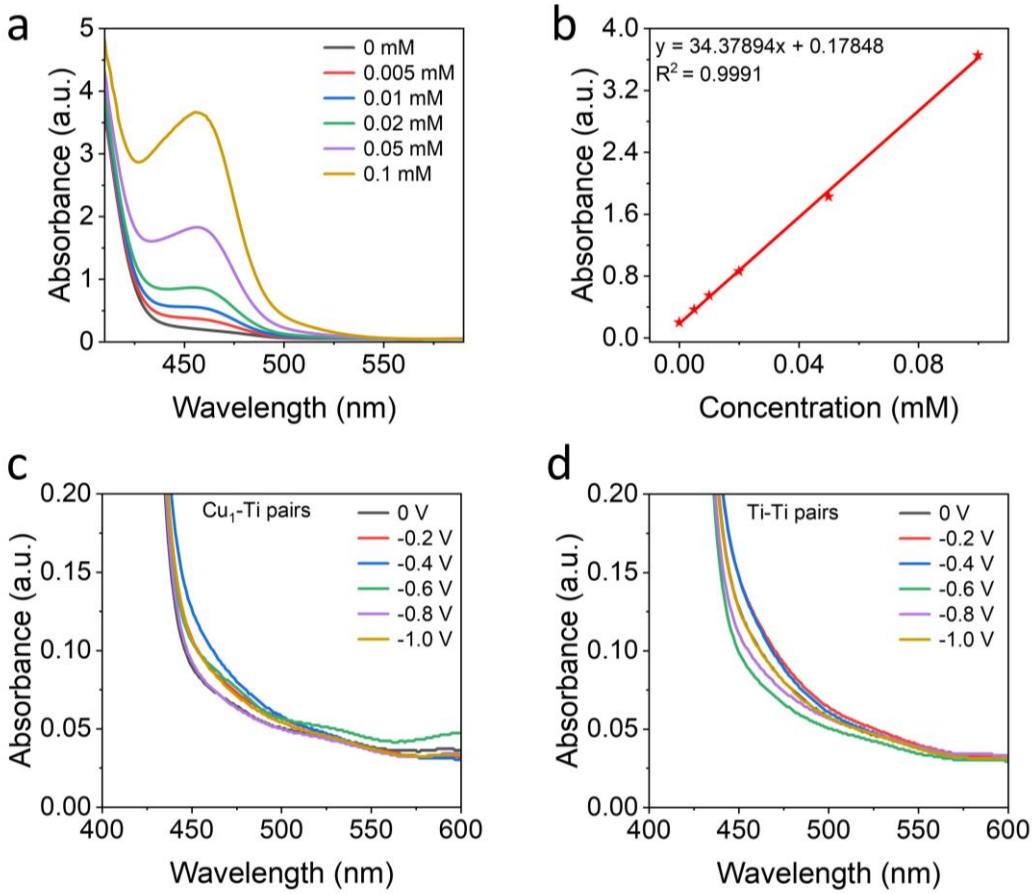

Supplementary Fig. 22 (a) UV-Vis absorption spectra of N_2H_4 assays. (b) Calibration curve for quantitative calculation of N_2H_4 concentrations. UV-Vis spectra for N_2H_4 produced by (c) Cu_1−Ti pairs and (d) Ti−Ti pairs. Source data for Supplementary Fig. 22 are provided as a Source Data file.

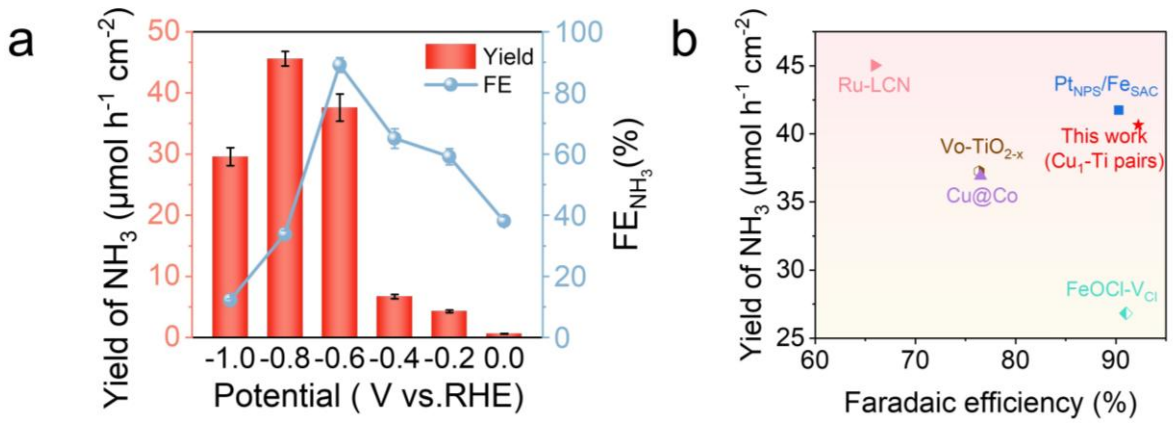

Supplementary Fig. 23 (a) NH_3 yield rates and FE_{NH3} of Cu_1–Ti pairs in 1 vol% NO-saturated 0.25 M K_2SO_4. The error bars correspond to the standard deviation of three times of NORR measurements. (b) Comparisons of the NORR performance of Cu_1–Ti pairs with other previously reported electrocatalysts under 1 vol% NO/Ar. Source data for Supplementary Fig. 23 are provided as a Source Data file.

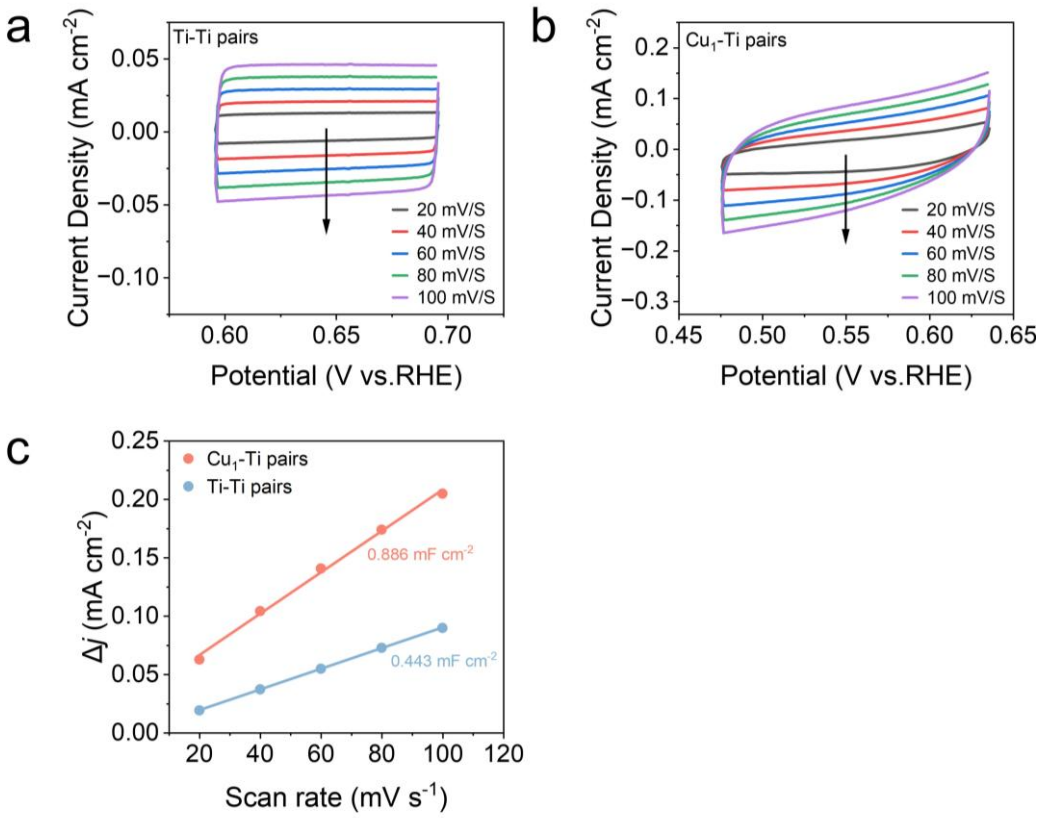

Supplementary Fig. 24 CV curves of (a) Ti−Ti pairs and (b) Cu_1−Ti pairs under different scan rates from 20 to 100 mV s^{-1}. (c) Plots of half of the current density difference ($\Delta j/2$) at the centered potential plotted against the scan rate. The slope of the fitted straight line is the electrical double-layer capacitor value. Source data for Supplementary Fig. 24 are provided as a Source Data file.

Determination of Double-Layer Capacitance (C_{dl}): As described in the main text (Electrochemical measurement), cyclic voltammetry (CV) scans were performed in a non-Faradaic potential region at various scan rates (20, 40, 60, 80, 100 mV s^{-1}). Subsequently, plot a scatter diagram with the scanning speed as the horizontal axis and the current density difference (Δj) at the voltage center as the vertical axis. The slope of the linear fit represents $2*C_{dl}$. As shown in Supplementary Fig. 24c, the specific capacitance of the Cu_1−Ti pairs and Ti−Ti pairs were 0.886 mF cm^{-2} and 0.443 mF cm^{-2}, respectively.

Calculation of Electrochemical Active Surface Area (ECSA): The ECSA was calculated using the

formula: ECSA = C_{dl} / C_s, where Cs denotes the specific capacitance. For a flat surface, Cs is generally found to be in the range of 20~60 μF cm^{-2}. In the following calculations of the electrochemically active surface area, we assumed that the Cs was 40 μF cm^{-2}, and the ECSAs of the two samples were calculated as follows:

$$A_{ECSA}^{Cu_1\text{-Ti pairs}} = \frac{0.886\ mF\ cm^{-2}}{40\ \mu F\ cm^{-2}\ per\ cm^2_{ECSA}} = 22.15\ cm^2_{ECSA}$$

$$A_{ECSA}^{Ti\text{-Ti pairs}} = \frac{0.443\ mF\ cm^{-2}}{40\ \mu F\ cm^{-2}\ per\ cm^2_{ECSA}} = 11.08\ cm^2_{ECSA}$$

The ECSA-normalized activity was calculated as follows:

$$\text{ECSA-normalized activity } (Cu_1\text{-Ti pairs}) = \frac{189.9\ \mu mmol\ h^{-1}\ cm^{-2} * 4\ cm^2}{22.15\ cm^2_{ECSA}}$$

$$= 34.29\ \mu mmol\ h^{-1}\ cm^{-2}_{ECSA}$$

$$\text{ECSA-normalized activity (Ti-Ti pairs)} = \frac{58.5\ \mu mmol\ h^{-1}\ cm^{-2} * 4\ cm^2}{11.08\ cm^2_{ECSA}}$$

$$= 21.13\ \mu mmol\ h^{-1}\ cm^{-2}_{ECSA}$$

Therefore, the resulting ECSA-normalized activity of the Cu_1−Ti pairs was 1.6 times greater than that of the Ti−Ti pairs.

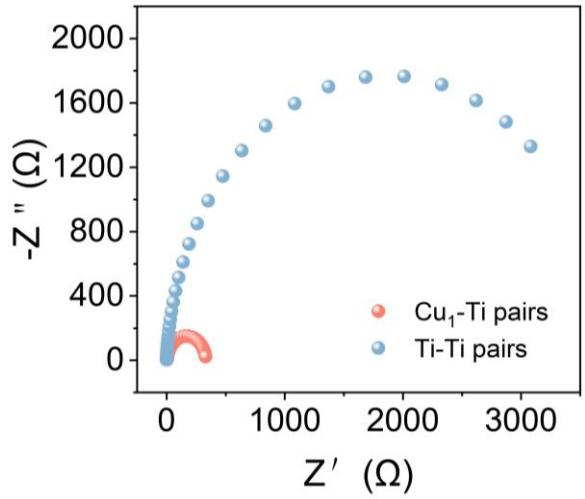

Supplementary Fig. 25 Electrochemical impedance spectroscopy (EIS) Nyquist plots of the Ti−Ti pairs and Cu_1−Ti pairs. Source data for Supplementary Fig. 25 are provided as a Source Data file.

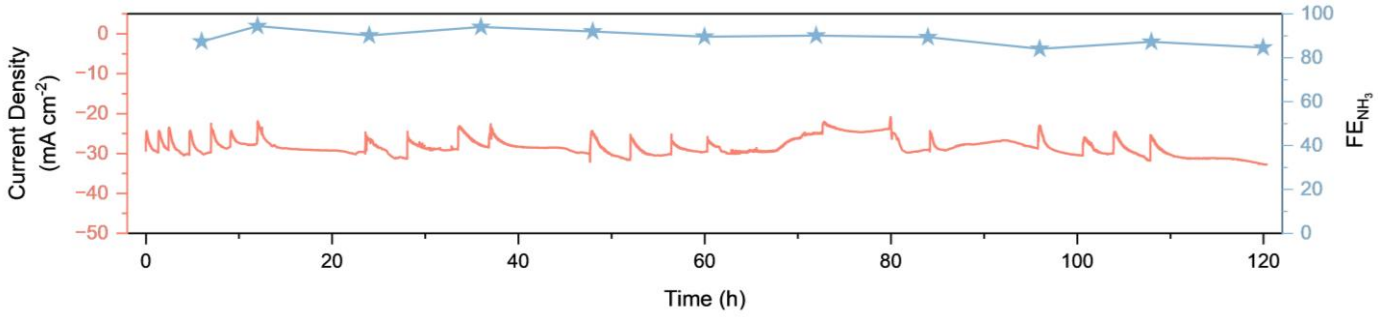

Supplementary Fig. 26 Long-term chronoamperometry test of Cu_1–Ti pairs at −0.6 V vs. RHE. Fluctuations in current density are attributed to a drop in the liquid level caused by sampling during the NORR process, coupled with the formation and detachment of bubbles on the electrode surface. Source data for Supplementary Fig. 26 are provided as a Source Data file.

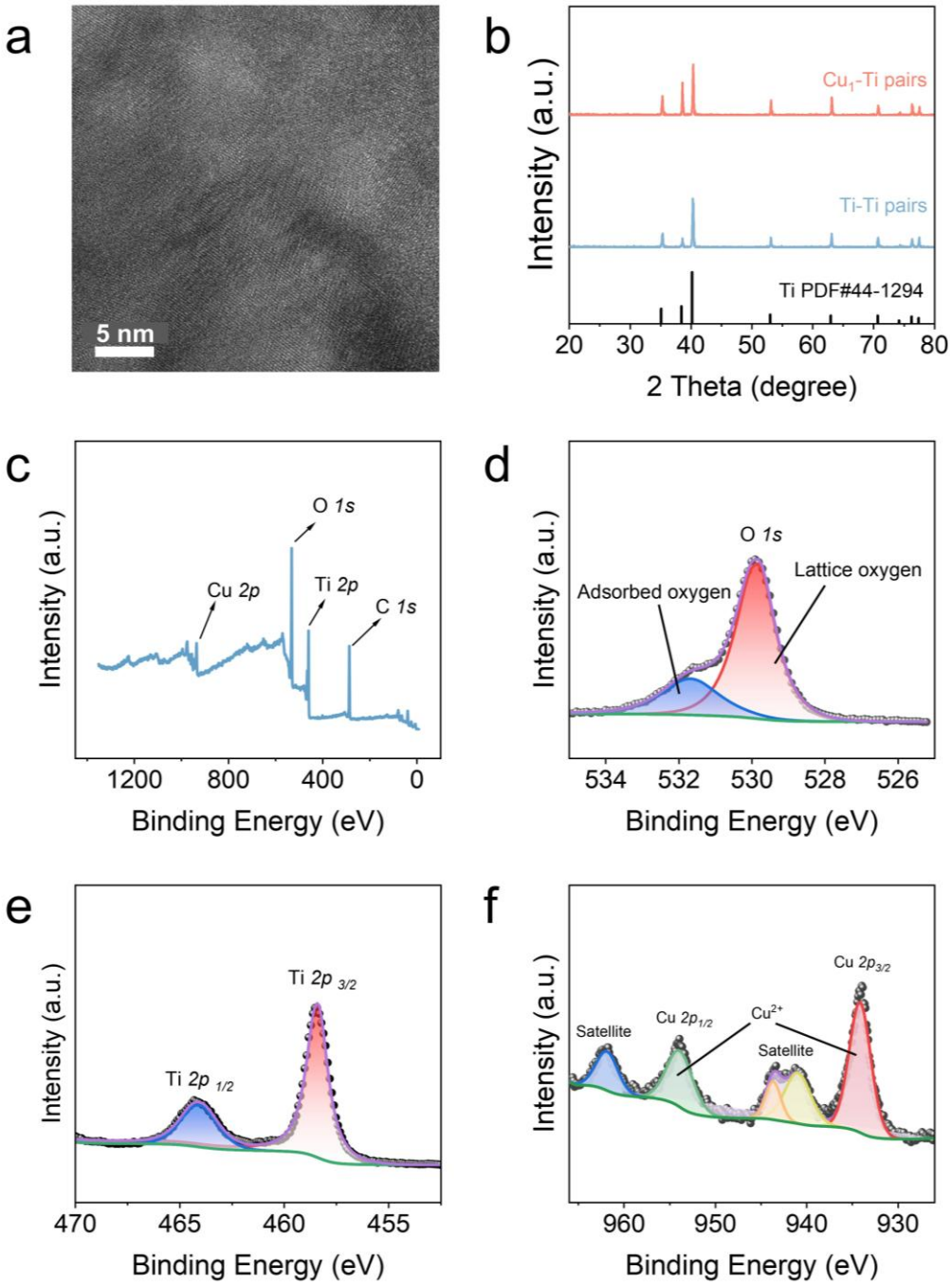

Supplementary Fig. 27 The HRTEM (a), XRD (b), and XPS (c, d, e, f) spectra of Cu_1−Ti pairs after cycling tests, suggesting the morphology or valence states of Cu and Ti species showed negligible changes. Source data for Supplementary Fig. 27 are provided as a Source Data file.

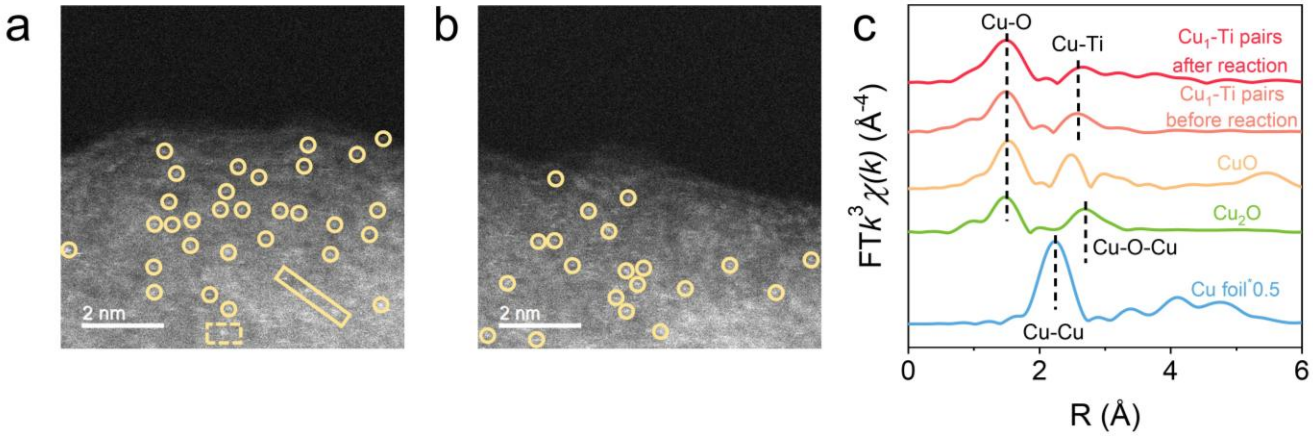

163

164 **Supplementary Fig. 28** The HAADF-STEM images of the Cu_1−Ti pairs (a) before testing and (b) after testing.

165 (c) FT EXAFS spectra at the Cu K-edge for Cu_1–Ti pairs before and after the reaction. Source data for

166 Supplementary Fig. 28 are provided as a Source Data file.

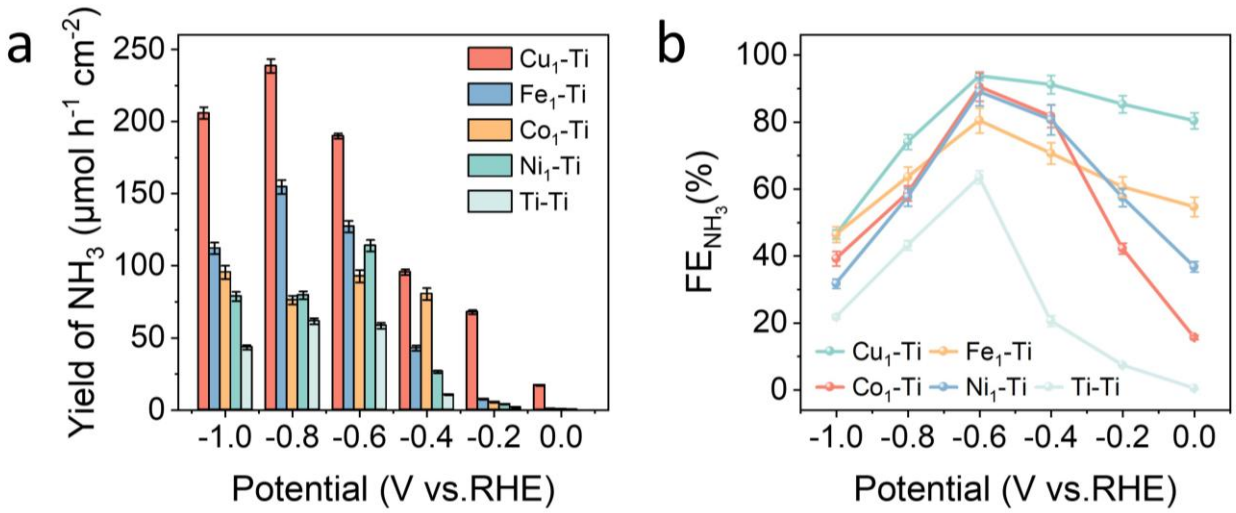

Supplementary Fig. 29 (a) NH_3 yield rate of Cu_1−Ti, Fe_1−Ti, Co_1−Ti, Ni_1−Ti and Ti−Ti at different potentials. (b) NH_3 FEs of Cu_1−Ti, Fe_1−Ti, Co_1−Ti, and Ni_1−Ti and Ti−Ti at different potentials. The error bars correspond to the standard deviation of three times of NORR measurements. Source data for Supplementary Fig. 29 are provided as a Source Data file.

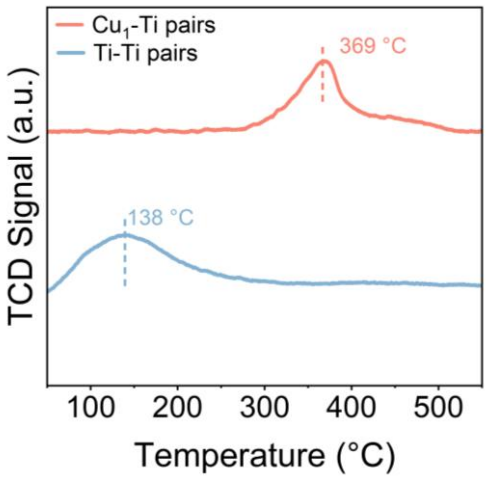

Supplementary Fig. 30 NO-TPD profiles of Ti−Ti pairs and Cu_1−Ti pairs. Source data for Supplementary Fig. 30 are provided as a Source Data file.

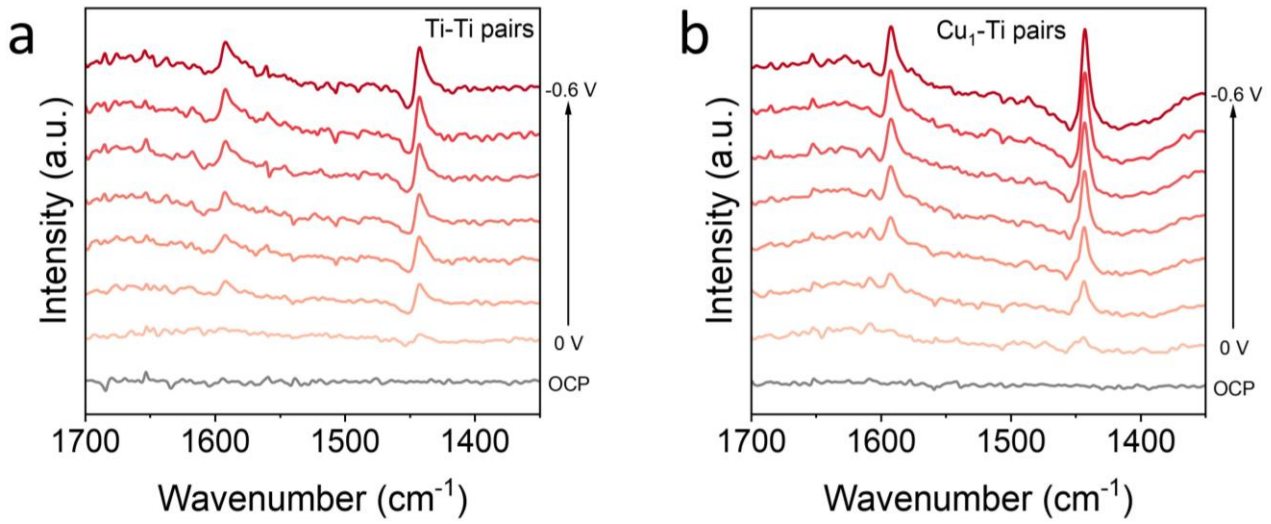

Supplementary Fig. 31 *In situ* pyrrole infrared spectroscopy reveals that the peak at 1445 cm^{-1} (Py on Mn^{+}) for Cu_1−Ti pairs is significantly stronger than that for Ti−Ti pairs, confirming that the introduction of Cu increases the Lewis acid sites. Source data for Supplementary Fig. 31 are provided as a Source Data file.

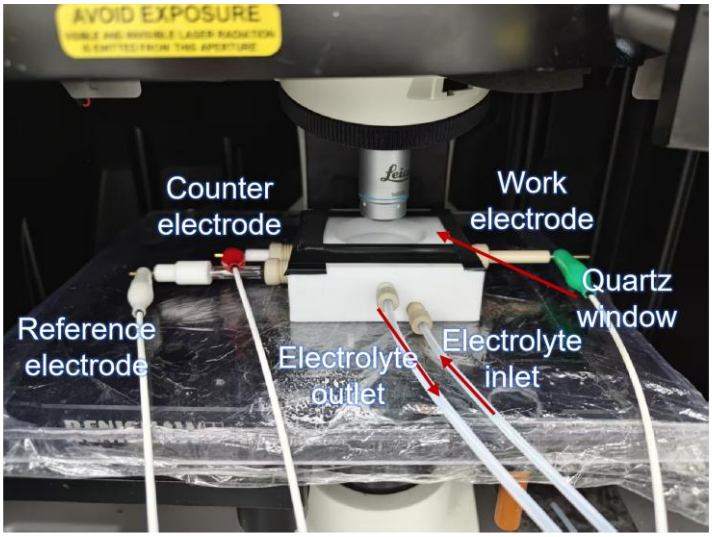

Supplementary Fig. 32 Digital photo of *in situ* electrochemical Raman measurement. The three-electrode system consists of a working electrode, a Pt foil counter electrode, and an Ag/AgCl reference electrode. The integrated electrolyte inlet and outlet ports enable continuous flow of NO-saturated electrolyte, with arrows denoting the direction of electrolyte flow. Black adhesive tape was used to hermetically seal the interface between the quartz glass window and the electrolytic cell to prevent air ingress.

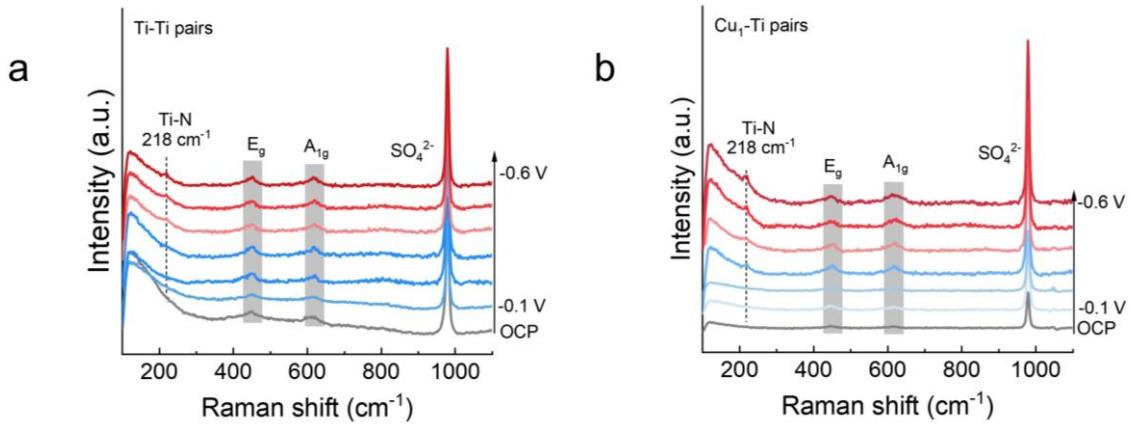

187

188 **Supplementary Fig. 33** *In situ* electrochemical Raman spectra of (a) Ti–Ti pairs and (b) Cu_1−Ti pairs during

189 the NORR in 0.25 M K_2SO_4. Source data for Supplementary Fig. 33 are provided as a Source Data file.

190

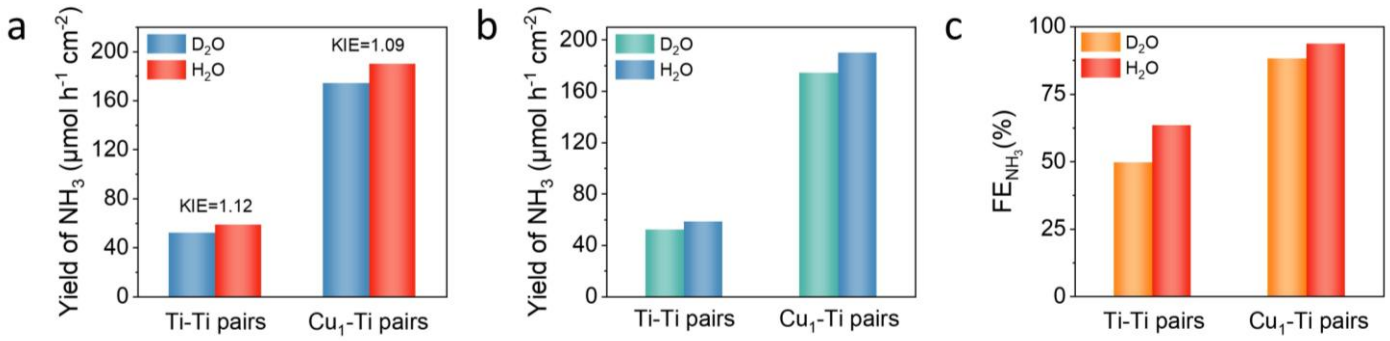

Supplementary Fig. 34 (a) Plot of the ratio of NH_3 production rate constant (KIE = k_{H2O}/k_{D2O}) on Ti−Ti pairs and Cu_1−Ti pairs The NH_3 yields (b) and FE_{NH3} (c) of Ti−Ti pairs and Cu_1−Ti pairs in H_2O and D_2O. Source data for Supplementary Fig. 34 are provided as a Source Data file.

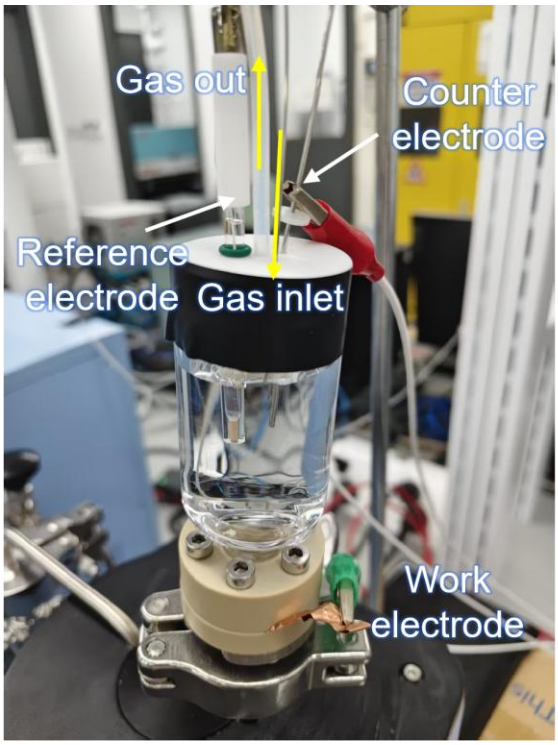

Supplementary Fig. 35 Digital photo of electrochemical *in situ* DEMS measurement. The three-electrode system consists of a working electrode, a Pt wire counter electrode, and an Ag/AgCl reference electrode. The gas inlet and outlet enable continuous gas flow, with arrows indicating the flow direction of NO. Black adhesive tape was applied to hermetically seal the interface between the quartz glass electrolytic cell and the PTFE bottle cap to prevent air ingress.

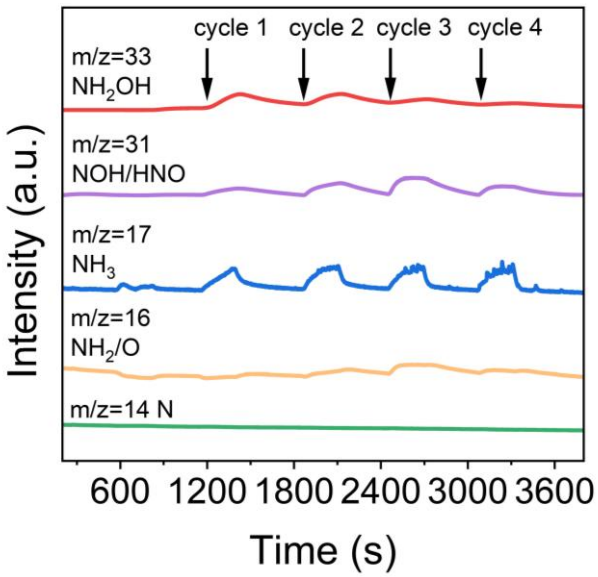

Supplementary Fig. 36 DEMS signals of the intermediates during the NORR of Ti−Ti pairs. Source data for Supplementary Fig. 36 are provided as a Source Data file.

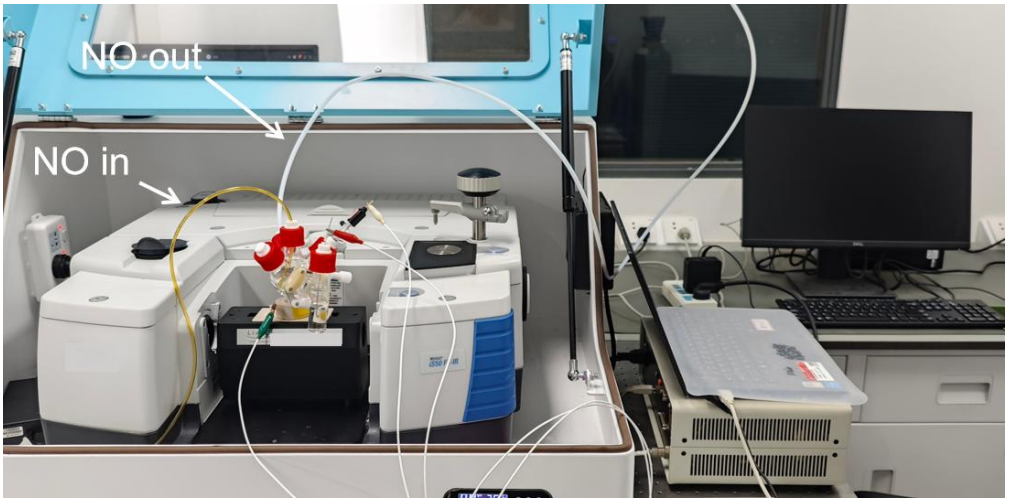

Supplementary Fig. 37 Digital photo of electrochemical *in situ* ATR-IR measurement.

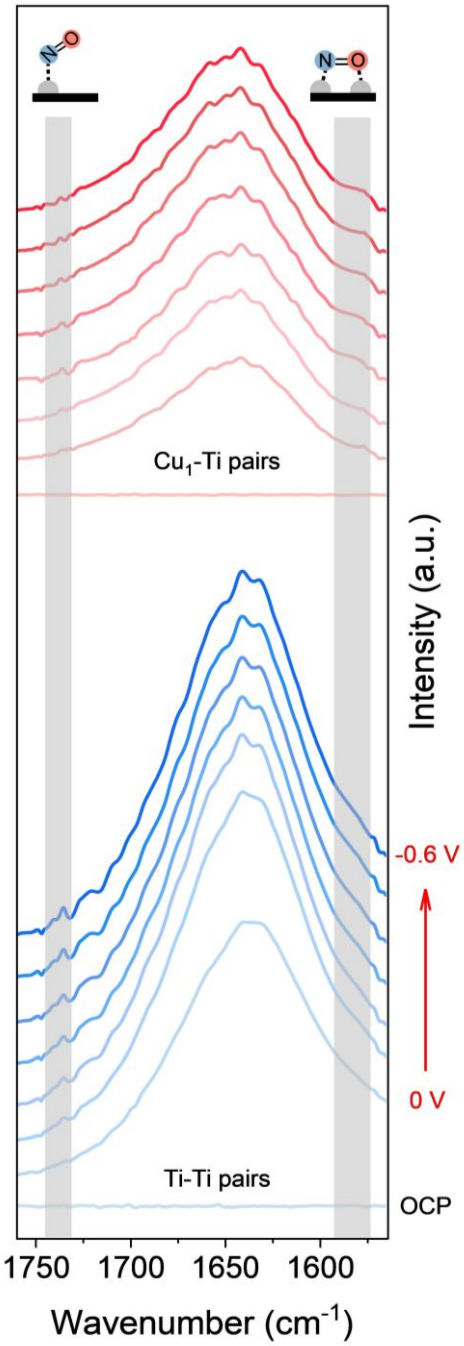

208

209 **Supplementary Fig. 38** *In situ* ATR-IRAS spectra (1560−1750 cm^{-1}) of Ti−Ti pairs and Cu_1−Ti pairs at various

210 potentials. Source data for Supplementary Fig. 38 are provided as a Source Data file.

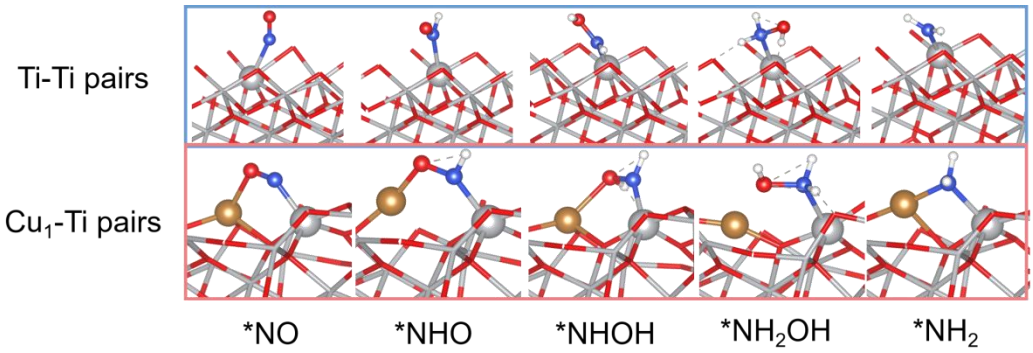

Supplementary Fig. 39 Optimized structures of intermediates for NORR on Ti−Ti pairs and Cu_1−Ti pairs. Gray, red, orange, blue and white balls represent Ti, O, Cu, N and H, respectively.

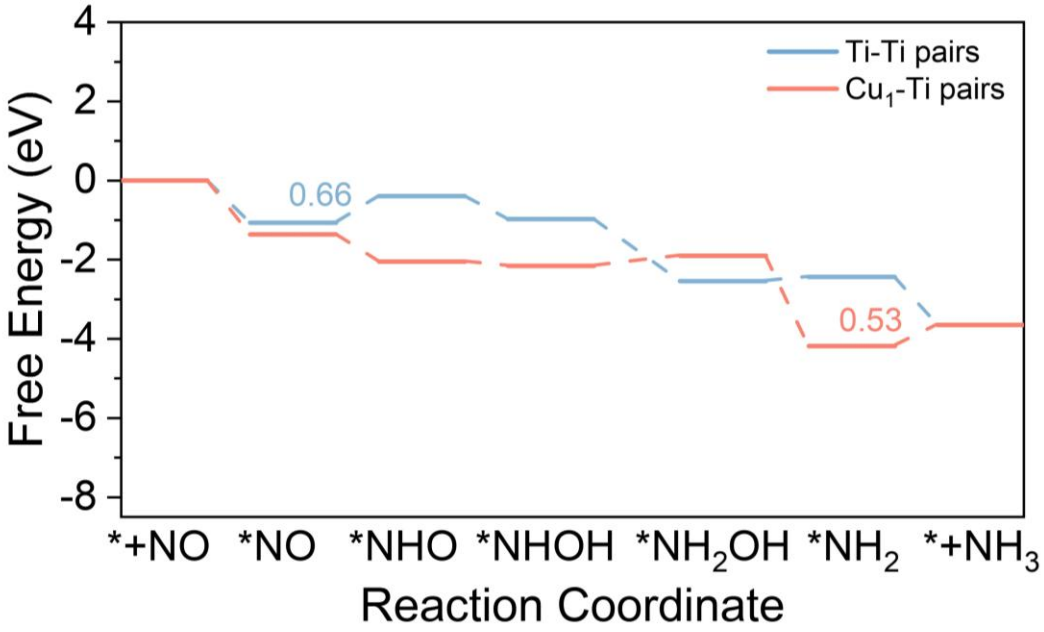

Supplementary Fig. 40 Free energy diagrams for NORR on Ti−Ti pairs and Cu_1−Ti pairs. Source data for Supplementary Fig. 40 are provided as a Source Data file.

Supplementary Tables

Supplementary Table 1. The fitted EXAFS data for Cu foil and Cu_1−Ti pairs samples.

Samples	Path	N	R (Å)	σ^2 ($Å^{-2}$)	ΔE_0 (eV)	R-factor
Cu foil	Cu-Cu	12	2.54 ± 0.01	0.0087	4.3 ± 0.5	0.0033
Cu_1−Ti pairs	Cu-O	3.90 ± 0.20	1.96 ± 0.01	0.0062	−3.6 ± 1.1	0.0114
	Cu-Ti	5.00 ± 0.60	3.02 ± 0.01	0.0150		
	(Cu-O-Ti)					

N is the coordination number; R is the interatomic distance (the bond length between central atoms and surrounding coordination atoms); σ^2 is the Debye-Waller factor (a measure of thermal and static disorder in absorber-scatterer distances); ΔE_0 is the inner potential correction; the R factor is used to value the goodness of the fitting. Error bounds that characterize the structural parameters obtained by EXAFS spectroscopy were estimated as CN ± 20%, R ± 1%; σ^2 ± 20%.

Supplementary Table 2. Comparison of NH_3 synthesis performance from NO electroreduction over Cu_1−Ti pairs and other reported catalysts.

Catalysts	Eletrolyte	Reactor type	NO/Ar (v/v)	Potential (V vs. RHE)	Yield rate (μmol cm^{-2} h^{-1})	FE_{NH3} (%)	Ref.
Cu_1−Ti pairs	0.25 M K_2SO_4	H-type cells	20%	-0.6	189.9	93.7	**This work**
Cu_1−Ti pairs	0.25 M K_2SO_4	H-type cells	1%	-0.6	37.59	89.1	**This work**
$Ru_{0.05}Cu_{0.95}$	0.5 M Na_2SO_4	H-type cells	25%	-0.5	17.68	64.9	[1]
bcc RuGa	0.1 M K_2SO_4	H-type cells	20%	-0.2	160.3	72.3	[2]
MoS_2/GF	HCl+0.5 mM Fe(II)SB	H-type cells	10%	-0.7	99.6	77.6	[3]
FeP/CC	0.2 M PBS	H-type cells	10%	-0.3	85.62	88.49	[4]
MnO_{2-x} NA/TM	0.2 M Na_2SO_4	H-type cells	10%	-0.7	82.8	9.9	[5]
HCNF/CP	0.2 M Na_2SO_4	H-type cells	10%	-0.6	22.35	88.33	[6]
CoS_{1-x}/CP	0.2 M Na_2SO_4	H-type cells	10%	-0.4	44.67	53.62	[7]

Bi NDs	0.1 M Na_2SO_4	H-type cells	10%	-0.5	28.8	89.2	[8]
NiO/TM	0.1 M Na_2SO_4	H-type cells	10%	-0.6	125.3	90	[9]
Cu@Cu/C NWAs	0.05 M H_2SO_4	H-type cells	3%	-0.1	69.4	93	[10]
Ru-LCN	0.5 M Na_2SO_4	H-type cells	1%	-0.2	22.51	65.96	[11]
Cu@Co	0.1 M Na_2SO_4	H-type cells	1%	-0.5	36.89	76.54	[12]
Pt_{NPs}/Fe_{SAC}	0.5 M K_2SO_4 + 50 mM SB	H-type cells	1%	-0.5	41.75	90.3	[13]
FeOCl-V_{Cl}	0.1 M HCl+50 mM SB	H-type cells	1%	-0.5	26.79	91.06	[14]
CuFe DS/NC	0.1 M Na_2SO_4	H-type cells	99%	-0.6	112.52	90	[15]
hcp-Co	0.1 M Na_2SO_4	H-type cells	99%	-0.6	439.5	72.58	[16]

226

Supplementary Table 3. Calculated ΔE, Δ_{ZPE}, TΔS and ΔG for each intermediate of the NORR pathway on the Ti–Ti pairs and Cu_1–Ti pairs catalyst.

		ΔE (eV)	Δ_{ZPE} (eV)	TΔS (eV)	ΔG (eV)
Ti–Ti pairs	*NO	-1.67	0.22	0.11	-1.06
	*NHO	-1.20	0.47	0.18	-0.40
	*HNOH	-2.12	0.78	0.12	-0.98
	*NH_2OH	-3.98	1.08	0.12	-2.54
	*NH_2	-3.54	0.65	0.11	-2.44
Cu_1–Ti pairs	*NO	-1.90	0.17	0.14	-1.36
	*NHO	-2.90	0.48	0.13	-2.05
	*HNOH	-3.30	0.79	0.15	-2.16
	*NH_2OH	-3.34	1.13	0.21	-1.90
	*NH_2	-5.35	0.70	0.08	-4.18

References

1. Shi J, *et al.* Promoting nitric oxide electroreduction to ammonia over electron-rich Cu modulated by Ru doping. *Sci China:Chem* **64**, 1493-1497 (2021).
2. Zhang H, *et al.* Isolated electron-rich ruthenium atoms in intermetallic compounds for boosting electrochemical nitric oxide reduction to ammonia. *Angew Chem, Int Ed* **135**, e202213351 (2023).
3. Zhang L, *et al.* High-performance electrochemical NO reduction into NH_3 by MoS_2 nanosheet. *Angew Chem, Int Ed* **133**, 25467-25472 (2021).
4. Liang J, *et al.* FeP nanorod array: A high-efficiency catalyst for electroreduction of NO to NH_3 under ambient conditions. *Nano Res* **15**, 4008-4013 (2022).
5. Li Z, *et al.* MnO_2 nanoarray with oxygen vacancies: An efficient catalyst for NO electroreduction to NH_3 at ambient conditions. *Mater Today Phys* **22**, 100586 (2022).
6. Ouyang L, *et al.* High-efficiency NO electroreduction to NH_3 over honeycomb carbon nanofiber at ambient conditions. *J Colloid Interface Sci* **616**, 261-267 (2022).
7. Zhang L, *et al.* Enhancing electrocatalytic NO reduction to NH_3 by the CoS nanosheet with sulfur vacancies. *Inorg Chem* **61**, 8096-8102 (2022).
8. Lin Y, *et al.* Bi nanodendrites for highly efficient electrocatalytic NO reduction to NH_3 at ambient conditions. *Mater Today Phys* **22**, 100611 (2022).
9. Liu P, *et al.* High-performance NH_3 production via NO electroreduction over a NiO nanosheet array. *Chem Commun* **57**, 13562-13565 (2021).
10. Meng J, Cheng C, Wang Y, Yu Y, Zhang B. Carbon support enhanced mass transfer and metal–support interaction promoted activation for low-concentrated nitric oxide electroreduction to ammonia. *J Am Chem Soc* **146**, 10044-10051 (2024).

11. Li Y, *et al.* Electrocatalytic reduction of low-concentration nitric oxide into ammonia over Ru nanosheets. *ACS Energy Lett* **7**, 1187-1194 (2022).

12. Wu Z, *et al.* Cu@ Co with Dilatation Strain for High-Performance Electrocatalytic Reduction of Low-Concentration Nitric Oxide. *Adv Mater* **36**, 2309470 (2024).

13. Guo X, *et al.* Electrosynthesis of NH_3 from low-concentration NO on cascade dual-site catalysts in neutral media. *Nat Commun* **16**, 8481 (2025).

14. Guo X, *et al.* Aqueous electroreduction of nitric oxide to ammonia at low concentration via vacancy engineered FeOCl. *Angew Chem, Int Ed* **136**, e202318792 (2024).

15. Wang D, *et al.* Oxygen-bridged copper–iron atomic pair as dual-metal active sites for boosting electrocatalytic NO reduction. *Adv Mater* **35**, 2304646 (2023).

16. Wang D, *et al.* Hexagonal cobalt nanosheets for high-performance electrocatalytic NO reduction to NH_3. *J Am Chem Soc* **145**, 6899-6904 (2023).